PCCP

Accepted Manuscript

Journal Name

Evolution of Jahn-Teller Distortion, Transport and Dielectric Properties with Doping in Perovskite NdFe$_{1-x}$Mn$_x$O$_3$ ($0 \leq x \leq 1$) Compounds [†]

Tirthankkar Chakraborty,[a$] Ruchika Yadav,[a*] Suja Elizabeth[a†] and H.L. Bhat[a‡]

We have carried out dielectric and transport measurements in NdFe$_{1-x}$Mn$_x$O$_3$ ($0 \leq x \leq 1$) series of compounds and studied the variation of activation energy due to change in Mn concentration. Despite similar ionic radii in Mn^{3+} and Fe^{3+}, large variation is observed in the lattice parameters and a crossover from dynamic to static Jahn-Teller distortion is discernible. The Fe/Mn-O-Fe/Mn bond angle on *ab* plane shows anomalous change with doping. With increase in Mn content, the bond angle decreases till $x = 0.6$; beyond this, it starts rising until $x = 0.8$ and again falls after that. A similar trend is observed in activation energies estimated from both transport and dielectric relaxation by assuming small polaron hopping (SPH) model. Impedance spectroscopy measurements delineates grain and grain boundary contributions separately both of which follow SPH model. Frequency variation of dielectric constant is in agreement with modified Debye law from which relaxation dispersion is estimated.

[a] *Department of Physics, Indian Institute of Science, Bangalore 560012, India. Fax: +91 (80) 2360 2602; Tel: +91 (80) 2360 2721*

[$] *E-mail: tirtha255@gmail.com; tirthankar@physics.iisc.ernet.in*

[*] *E-mail: ruchika@physics.iisc.ernet.in*

[†] *E-mail: liz@physics.iisc.ernet.in*

[‡] *Centre for Nano and Soft Matter Science, Bangalore-560013, India, E-mail: hlbhat@physics.iisc.ernet.in*

1 Introduction

The giant magnetoresistance and magnetodielectric effect have attracted considerable research interest during last few years mainly because of their applicability in electronic switches, sensors, actuators and memory devices [1–7]. Materials with coupled magnetic and electric order parameters resulting extra degree of freedom hold prospects for new generation memory devices. In particular, magneto-electric multiferroics have an edge [8,9]. Unfortunately, in most reported materials, the coupling is either very weak or appears at low temperature which poses a challenge to their applicability at room temperature. Besides multiferroics, other materials also offer a choice with optimum magnetic and electric order parameter coupling at room temperature. Systems with electric properties related to structural changes and associated magnetic properties appear interesting. Rare earth orthoferrites RFeO$_3$ are well known for their high Neel temperature ($T_N \sim 620$ K) and spin reorientation in the low temperature region [10–13]. In RFeO$_3$ perovskites, Fe^{3+} [3d^5] has electronic configuration $t_{2g}^3 e_g^2$ with both the e_g orbitals namely $3x^2 - r^2/3y^2 - r^2$ and $y^2 - z^2/x^2 - z^2$ filled. These have half-filled d orbitals and adopt G-type antiferromagnetic structure arising from strong Fe^{3+}-O-Fe^{3+} antiferromagnetic coupling in all directions in accordance with Goodenough-Kanamori rule. In RMnO$_3$ manganites, Mn^{3+} [3d^4] has electronic configuration $t_{2g}^3 e_g^1$ in high spin and is Jahn-Teller distorted in the

crystal field of MnO_6 octahedra. Kanamori[14] showed that static cooperative Jahn-Teller distortion gives rise to three different Mn-O bond lengths, long (*l*), middle (*m*) and short (*s*). To minimize the elastic energy, Goodenough[15] proposed cooperative orbital ordering for $LaMnO_3$. Staggered orbital ordering, where *l* and *s* bonds alternate on (001) plane and all *m* bonds are along [001] direction, has been observed in neutron diffraction study in $LaMnO_3$[16,17]. This is expected to be present in all $RMnO_3$ with larger size cation (R) and also in $NdMnO_3$. Whereas the t_{2g} orbitals are half filled, on (001) or *ab* plane, the $3x^2 - r^2/3y^2 - r^2$ of e_g orbitals are alternately filled and $y^2 - z^2/x^2 - z^2$ of that are empty. As a result, Mn^{3+}-O-Mn^{3+} bonds consist of different types of exchange interaction along different directions. Along *c* axis, e_g orbitals with their empty $y^2 - z^2/x^2 - z^2$ orbitals, lead to $e_g^0 - O - e_g^0$ anti exchange interaction in accordance with Goodenough-Kanamori rule. Moreover, $t_{2g}^3 - O - t_{2g}^3$ interaction exists which is antiferromagnetic causing the resultant interaction along *c* axis also to be antiferromagnetic. On the *ab* plane, the coupling between half filled $3x^2 - r^2/3y^2 - r^2$ and empty $x^2 - z^2/y^2 - z^2$ yields $e_e^1 - O - e_g^0$ coupling which is ferromagnetic whereas, the $t_{2g}^3 - O - t_{2g}^3$ coupling is antiferromagnetic. For larger size of R cation, the former dominates the *ab* plane and the system adopts A-type antiferromagnetic structure[16,18]. Since Fe^{3+} and Mn^{3+} have similar ionic radii, Mn^{3+} substitution in B site of $NdFeO_3$ will not result in structural distortion. But, since orthoferrites and manganites have different magnetic interactions, magnetic interaction in $NdFeO_3$ is likely to be modified with Mn doping. As an example, the orbital ordering in 50% doped FeMn system has been predicted[19]. Two out of four nearest neighbor Fe/Mn-O-Mn/Fe ($e_g^1 - O - e_g^0$) interactions are ferromagnetic on *ab* plane, and the other two are antiferromagnetic ($e_g^1 - O - e_g^1$). This is considerably different from both pure orthoferrites and manganites where all four interactions on *ab* plane are antiferromagnetic and ferromagnetic respectively for large R cation as well as Nd. Competition between ferromagnetic and antiferromagnetic interactions on *ab* plane is expected in mixed Fe-Mn systems and the magnetism varies with doping concentration. While we studied only the electric properties of a magnetic system, there are few other reports[20,21] which relate changes in structural and electric properties with magnetic structure. The study of structural changes and associated electric properties is considered significant as they are mediated by changes in

magnetic interaction in $NdFeO_3$ with Mn doping.

## 2 Experimental

The polycrystalline $NdFe_{1-x}Mn_xO_3$ ($0 \leq x \leq 1$) series (named as NFMO followed by *x* value in percent) of compounds were synthesized by conventional solid state reaction method. Stoichiometric ratio of highly pure (99.99%) precursors Nd_2O_3, Fe_2O_3 and MnO_2 were mixed thoroughly and sintered at 1100 ^{0}C and again at 1300 ^{0}C for 24 and 60 hours respectively with several intermediate grinding. The fraction of Mn content in each sample was verified with ICP-AES. Phase purity was checked using powder X-ray diffraction method in a diffractometer with Cu Kα source. Rietveld refinement using FullProf software was carried out on powder X-ray diffraction patterns to refine the structural parameters of as-grown samples. For pelletization, a small portion of the powdered sample mixed with a small amount of PVA, was pressed with 50 Kg/cm^2 pressure and then sintered at 1350 ^{0}C for 12 hours. Two probe resistivity method was applied to measure the resistivity of the pelletized samples. Temperature dependent dielectric measurement was done for all the samples at different frequencies (10 kHz, 20 kHz, 40 kHz, 100 kHz, 200 kHz, 400 kHz, 1 MHz, 2 MHz and 4 MHz) within the temperature range 300 K to 10 K in a closed cycle refrigerator with HP4275A LCR Meter. Dielectric response was recorded using frequency and temperature scans in the frequency range 100 Hz to 1 MHz at temperatures ranging from 300 K to 10 K using Agilent 4294A precision impedance analyzer. The impedance spectroscopic analysis was made using the software EIS Spectrum Analyser.

3 Results and discussion

3.1 Structural properties

Figure 1 gives the representative Rietveld refined pattern and the crysral structure of $NdFe_{0.5}Mn_{0.5}O_3$. It shows a distorted orthorhombic structure which refines in *Pbnm* space group. Similar structure is observed for other compounds of this series. The ionic radii of Fe^{3+} and Mn^{3+} are quite similar implying that the structure is not greatly distorted. Despite similar radii of B-site dopants, significant changes are observed in the lattice parameters with doping as shown in Fig. 2. The change in lattice parameters is a direct consequence of Jahn-Teller distortion and orbital ordering. As seen from Fig. 2, lattice parameters *a* and *c* decrease with increase in Mn content while *b* is invariant till
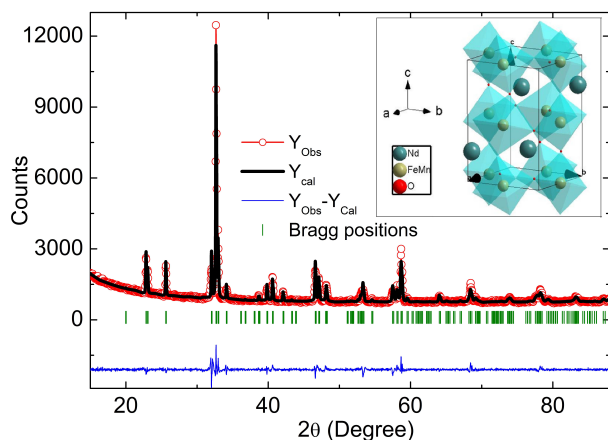
Fig. 1 Refinement of powder XRD pattern of $NdFe_{0.5}Mn_{0.5}O_3$. Inset shows the schematic unit cell of the same compound.
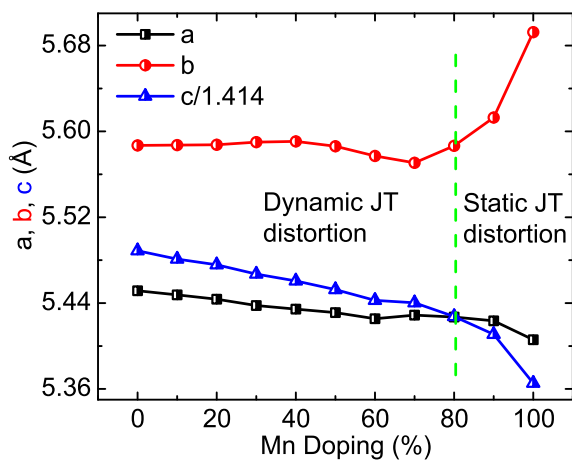

Fig. 2 Change in lattice parameters with Mn doping. Transfer from dynamic to static Jahn-Teller distortion is evident at 80% doping level.

about 50% Mn content and decreases slightly till $x = 70\%$. After this, b increases with Mn doping. In compounds with $x \leq 80\%$ O-orthorhombic structure is observed with $a < c/\sqrt{2} < b$ that transforms to O′-orthorhombic structure with $c/\sqrt{2} < a \leq b$[14] for $x > 80\%$. With increase of Mn content, the system becomes more Jahn-Teller distorted and, for $x \geq 80\%$ or higher, the system displays static Jahn-Teller distortion. Similar behavior was reported for other B-site doped compounds as well[20,21].

Bond angles and bond lengths also show significant dependence on Mn content. The variation of average Fe/Mn-O bond length on ab plane Fe/Mn-O-Fe/Mn (TM-O-TM)

bond angle is shown in Fig. 3. With increase in Mn doping, a minimum and maximum are observed in TM-O-TM at $x = 60\%$ and 80% respectively. TM-O-TM decreases till
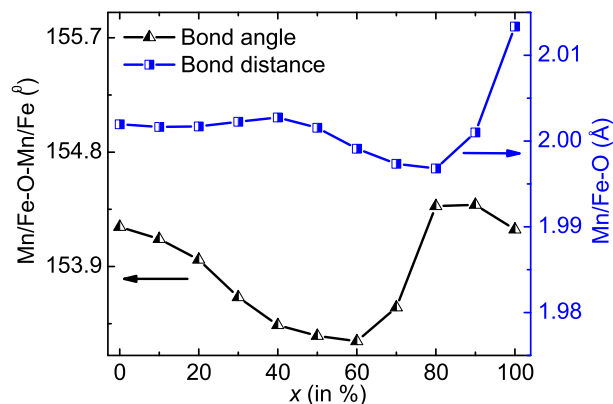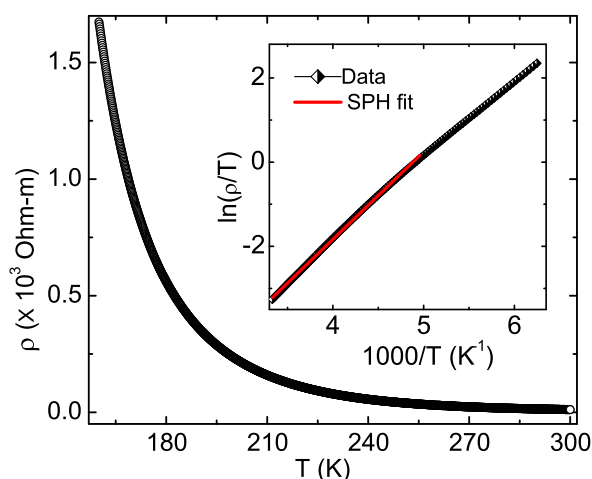

Fig. 3 Mn/Fe-O-Mn/Fe bond angle in ab plane and average Mn/Fe-O bond length.

$x = 60\%$ beyond which an abrupt increase in bond angle is observed reaching a maximum at $x = 80\%$. On further increasing the Mn content, bond angle shows slight decrease. A similar but complementary behavior is observed in the evolution of Fe/Mn-O bond length with doping. The bond length gradually increases till $x = 40\%$, and then, starts to decrease until a minimum value is reached for $x = 80\%$ when it sharply increases for Mn contents greater than 80%. The variation of bond length is related to the change in TM-O-TM bond angle. Decrease in bond angle results in elongation of the average Fe/Mn-O bond lengths in ab plane. Similar $GdFeO_3$ type distortion is seen in perovskite structure where TM-O-TM deviates from 180^0.

3.2 Transport properties

The transport properties of $NdFe_{1-x}Mn_xO_3$ series has been studied using two-probe resistivity measurement. It is seen that the resistivity of the samples decrease exponentially with increasing Mn content in the system. A small oxygen nonstoichiometry is commonly seen in perovskite oxides[22–24]. Oxygen vacancies appear during the cooling process of the compounds after they are annealed at high temperature,[25–28]. This, in turn, causes few Mn^{3+} ions to be transformed to Mn^{4+} to maintain charge neutrality. In this situation, double exchange (DE) interaction is possible within Mn^{3+}-O-Mn^{4+} clusters where the transfer of charge carriers occurs easily from one site to another. For samples

with low Mn content, there may be no or few small clusters of Mn^{3+}-O-Mn^{4+}. Hopping of charge carriers among Mn^{3+}-O-Mn^{4+} clusters is hindered by the majority of Fe^{3+} ions[24] and the resistivity becomes very high. When Mn content is less than 20%, the resistivity is beyond the instrument range ($\geq 100M\Omega$). All samples show insulating behavior where resistivity increases as the temperature is decreased. When Mn content increases, Mn clusters grow in size and the transport of the charge carriers within the system is easier. Hence, the resistivity of the system decreases for higher Mn content. In $NdMnO_3$, the resistivity can be measured up to the lowest temperature of about 160 K which is shown in Fig. 4. In mixed valence transition metal per-
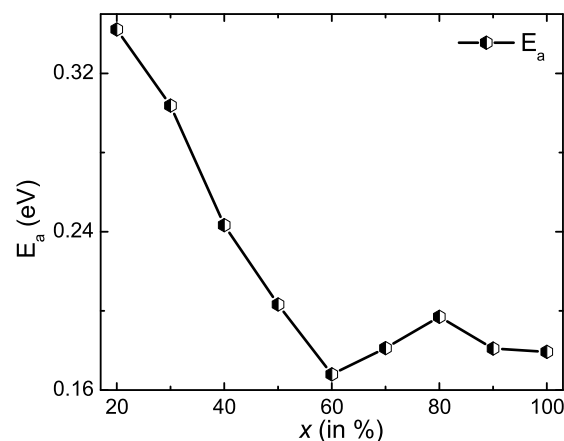

Fig. 5 Change of activation energy with Mn doping calculated from resistivity masurement with SPH model.

Fig. 4 Resistivity of $NdMnO_3$. Inset shows the fitting of resistivity using SPH model.

ovskite oxides, there are experimental evidences of small polarons[27,29]. In the present study, the resistivity was fitted with small polaron hopping (SPH) model. For SPH model, the temperature dependent resistivity is expressed as:

$$\rho = \rho_0 T \exp(E_a/k_B T) \tag{1}$$

where, E_a is the activation energy of small polarons to hop to their nearest neighboring sites and k_B is the Boltzmann constant. Using Eq. 1, the activation energies of all the samples were calculated. The variation of E_a with Mn content is shown in Fig. 5. It is noticed that this trend is quite similar to the change in Mn/Fe-O-Mn/Fe bond angle on ab plane with Mn content. With increasing Mn con-

tent, E_a decreases till $x = 60\%$, then rises. Beyond $x = 80\%$, it decreases slowly. Mn^{3+} ($3d^4$) has an electronic configuration ($t_{2g}^3 e_g^1$) of half-filled t_{2g} orbital and one empty e_g orbital while Fe^{3+} ($3d^5$) has half-filled t_{2g} and e_g orbitals with electronic configuration ($t_{2g}^3 e_g^2$). This results in stronger antiferrimagnetic interaction between Fe-O-Fe as compared to Mn-O-Fe antiferromagnetic interactions. As Mn content increases, the antiferromagnetic interactions in the system weakens. According to Goodenough-Kanamori-Anderson rule, superexchange antiferromagnetic interaction becomes stronger when the TM-O-TM bond angle approaches 180^0 [15,30–32]. This is reflected in Fig. 3 where bond angle decreases as the antiferromagnetic interaction of the system becomes weaker with increasing Mn content. From Fig. 2, one can deduce that there is no cooperative Jahn-Teller distortion and hence no orbital ordering in the system at Mn compositions less than 80%. In this situation, the system avails G-type antiferromagnetic ordering[20] which is observed in pure orthoferrite perovskites. Antiferromagnetic exchange interaction restricts electron transfer between two sites and, as it becomes weaker, the activation energy of the system decreases. G-type antiferromagnetic system leads to Dzyaloshinskii Moriya (DM) interaction which, in turn, causes spin canting and reduces the bond angle. Incorporation of Jahn-Teller active Mn^{3+} ions strengthens the Jahn-Teller distortion. For a threshold Mn content, it is considered that the system will facilitate or-

bital ordering among Mn rich clusters which is likely to favor A-type antiferromagnetic ordering. This process weakens the DM interaction as this is not favored in A-type antiferromagnetic ordering. Hence, the increase of bond angle for compounds beyond 60% Mn content can be attributed to gradual disappearance of the DM interaction. The activation energy increases as a consequence. Spin canting occurs since the probability of electron transfer between the two sites is large. When the Mn content is more than 80%, staggered orbital ordering occurs as a result of static Jahn-Teller distortion. This is clear in Fig. 2. In this case, A-type antiferromagnetic ordering is preferable and, on *ab* plane, $e_g^1 - O - e_g^0$ ferromagnetic interaction becomes strong. The overall antiferromagnetic interaction is weak as related by the gradual decrease of bond angle and activation energy beyond Mn composition of 80%.

3.3 Dielectric properties

Dielectric properties of all samples are compared to analyze the change with doping. When AC field is applied to a system, the polarization does not follow the field immediately. The lag between the change in polarization and electric field makes permittivity become a complex function as,

$$\varepsilon = \varepsilon' + i\varepsilon'' \tag{2}$$

where, ε' is the real part and ε'' is the imaginary part of the permittivity. The phase difference δ between the applied field $\mathbf{E}$ and the electric displacement vector $\mathbf{D}$ is given by $\tan\delta = \varepsilon''/\varepsilon'$.

The real part of dielectric constant $\varepsilon_r'(= \varepsilon'/\varepsilon_0)$ of all the samples at a particular frequency of 1 MHz (out of measurements made at nine different frequencies for each sample) is shown in Fig. 6. In all samples, on cooling, the decrease in ε_r' is followed by a plateau region and a peak in ε_r'' as well as in $\tan\delta$. The peak positions are frequency dependent which shift to high temperature with increasing frequency. This is characteristic of thermally activated relaxation in the system. The measured value of ε_r' depends on many experimental factors such as, preparation condition and environment, pelletization pressure etc. which have an impact on grain and grain boundaries and even on sample electrode interfaces. Hence, it is difficult to obtain consistency in absolute values of ε_r' with different doping levels at a fixed temperature. But the noticeable feature

is the temperature at which the peak in ε_r'' and $\tan\delta$ occurs. This moves to low temperatures with increasing Mn content (except NdMnO$_3$ for which it is equal to that of $x = 90\%$). It was already reckoned that Mn-O-Fe or Mn-O-Mn bond strengths are weaker than Fe-O-Fe bond strength. The weaker the bond, the easier it is for polarons to hop and follow the applied AC field up to low temperature even when the thermal energy is less. The activation energy of the relaxation is given by the Arrhenius equation,

$$f = f_0 \exp(-E_a/k_B T) \tag{3}$$

where, T corresponds to the position of maxima of $\tan\delta$ at frequency f and f_0 is the pre-exponential term. As stated above, the system follows SPH model and is seen to better follow the equation

$$f = \frac{f_0}{T} \exp(-E_a/k_B T) \tag{4}$$

which can be shown to be valid for our system [27].
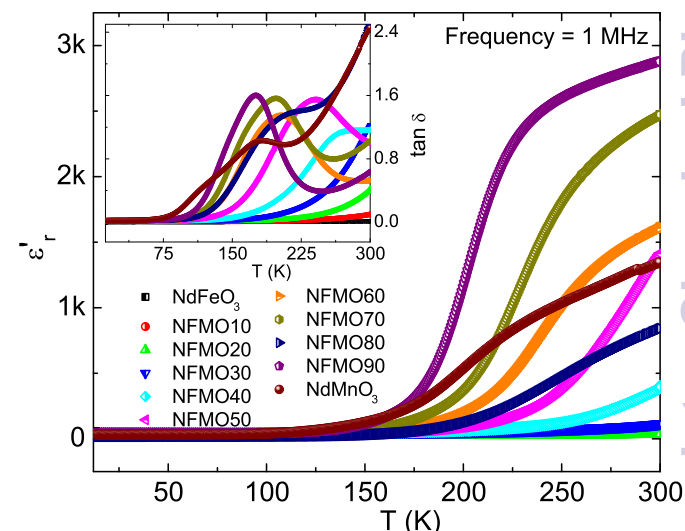
Fig. 6 Dielectric constant of all samples at a fixed frequency 1 MHz. Inset shows $\tan\delta$ for all the samples. The relaxation temperature decreases monotonically with increasing Mn content.

The variation of E_a with doping is shown in Fig. 7. The relaxation temperature in systems with x=0, 10 and 20% is beyond 300 K and hence E_a cannot not be measured in these. But for all other samples, the activation energy follows similar trend as is seen earlier in Fig. 5. The values

are quite close to that obtained from resistivity measurements. It is safe to assume that small polaronic hopping is responsible for both DC conductivity and dielectric polarization. In all samples, f_0 is of the order of 10^{14} which is in between that of free charge ($\sim 10^{16}$ Hz) and lattice or phononic relaxation ($\sim 10^{12}$ Hz). This is in consonance with other systems with polaron relaxation[26]
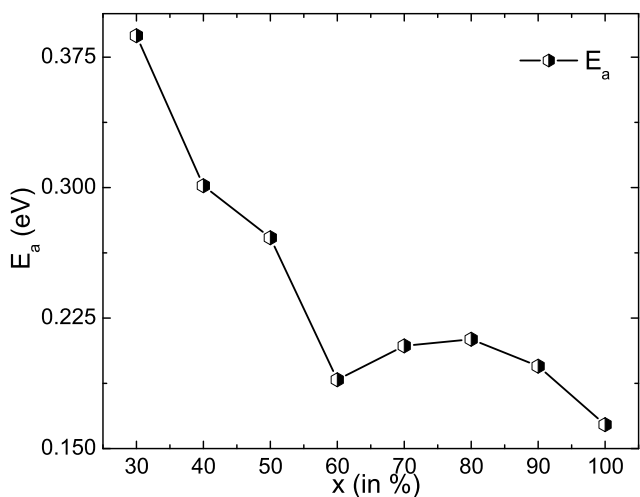
Fig. 7 Change in activation energy with doping calculated from dielectric relaxation using SPH model.

### 3.4 AC conductivity of NFMO50

To elucidate the transport phenomena, temperature dependent AC conductivity and dielectric response data were obtained on half-doped sample in the frequency range, 100 Hz to 1 MHz at the applied field of 500 mV. The AC conductivity is given by

$$\sigma_{ac}(\omega) = \varepsilon_0 \omega \varepsilon'' \qquad (5)$$

where, ε_0 is the free space permittivity and ε'' is the imaginary part of the dielectric constant. When the charge carriers hop between neighboring sites and drift long distance by hopping among localized states, hopping conduction results. Unlike DC transport phenomenon which responds to the applied electric field immediately, hopping charge transport is a relaxation process and results in current component in-phase and out-of-phase to electric field. Below a certain frequency ω_H, called the hopping frequency, the conductivity decreases due to charge accumulation at electrode and grain boundary interface. At low frequencies, the

hopping mechanism is not perturbed by electric field and the conduction is due to long range translational motion of the charge carriers. The conduction is almost independent of frequency and approximately equal to the DC value. So, the extrapolation of σ_{ac} in low frequency region gives the DC conductivity σ_{dc} at a particular temperature.

The frequency dependence of σ_{ac} at different temperatures is shown in Fig. 8. The AC conductivity can be explained
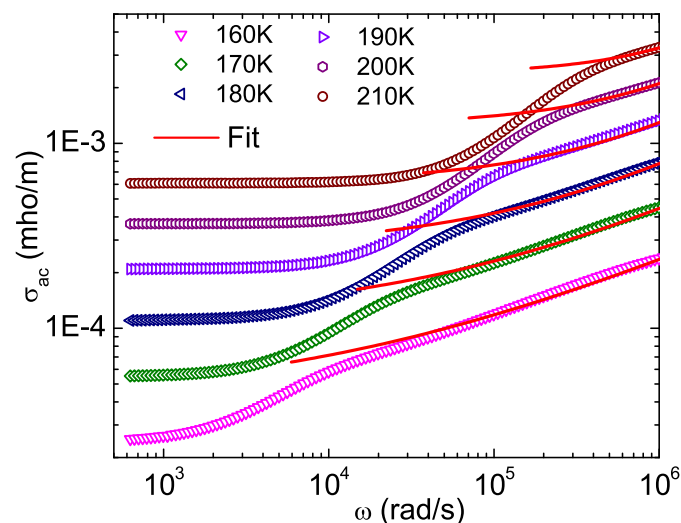
Fig. 8 Dependence of AC conductivity on frequency at different temperatures and fitting to Jonscher's power law.

by Jonscher's power law[33] as,

$$\sigma_{ac} = \sigma_{dc}[1 + (\omega/\omega_H)^n] \qquad (6)$$

where, n is a dimensionless exponent with $0 < n < 1$. As seen in Fig. 8, the experimental curves are marked by two regions. (1) A sharp rise region of σ_{ac} at low frequency due to grain boundary blocking effect and (2) A region at higher frequencies corresponding to bulk conductivity, here, σ_{ac} does not rise rapidly with frequency[27]. The high frequency region can be fitted by Jonscher's power law. The bulk DC conductivity σ_{dc} at different temperatures is obtained. σ_{dc} is seen to follow the SPH model by the expression,

$$\sigma_{dc} = \frac{\sigma_0}{T} \exp(-E_a/k_B T) \qquad (7)$$

where, E_a is the activation energy for hopping. The value of activation energy is found to be 0.22 eV.
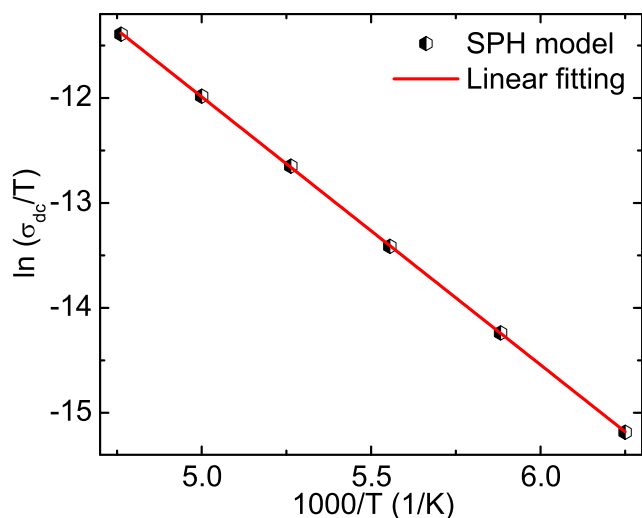
Fig. 9 SPH model fit of σ_{dc} according to equation 7.

3.5 Impedance spectroscopy of NFMO50

Impedance spectroscopy helps to visualize the grain and grain boundary effects in relation to the impedance which has usually has both resistive and reactive (due to capacitive/inductive effect) components. Both components are measurable as Z' and Z'' respectively. The complex impedance is then given by,

$$Z^* = Z' + Z'' \tag{8}$$

For ideal Debye type behavior where there is no interaction among the dipoles, the Z' vs. Z'' plot (Nyquist plot) is a perfect semicircle. In practice, the relaxation deviates from ideal Debye-type behavior. Moreover, because of the contributions from different regions -grain, grain boundary and sample electrode interface, the Nyquist plot becomes asymmetric. Generally, the number of the semicircles is equal to the number of relaxation in the system. Ideally, each relaxation can be represented with one RC equivalent circuit. A series of RC elements are used to represent (model) more than one relaxation and the impedance for ideal case is given by,

$$Z^* = \frac{R_1}{(1 + i\omega R_1 C_1)} + \frac{R_2}{(1 + i\omega R_2 C_2)} + \frac{R_2}{(1 + i\omega R_2 C_2)} + ... \tag{9}$$

where, ω is the angular frequency of the applied AC voltage. Due to nonideal behaviour of Z^*, constant phase ele-

ment (CPE) is used instead of ideal capacitor. The complex impedance of the CPE is given by,

$$Z^*_{CPE} = \frac{1}{C_{CPE}(i\omega)^n} \tag{10}$$

where, C_{CPE} is the specific capacitance of the CPE and $0.6 \leq n \leq 1$. By fitting the experimental impedance data using Eq. 9 with proper R-CPE elements, the corresponding resistance and capacitance values can be deduced. The high frequency response is generally dominated by the grain (or bulk), the intermediate frequency by the grain boundary and lower frequency by the sample electrode interface[34,35]. At room temperature, the contribution from the grain is not clear. But, it becomes more prominent at lower temperature. In the present study, the Nyquist plot at different temperatures was modeled with three R-CPE elements with resistances R_g, R_{gb}, R_{se} and CPEs C_g, C_{gb}, and C_{se} corresponding to the grain, grain boundary and sample electrode interface respectively along with one series resistance R_s. The equivalent circuit and the simulated curves superimposed over the experimental data at specific temperatures are illustrated in Fig. 10. In practice, R_{gb} is always greater than R_g at a particular temperature which can
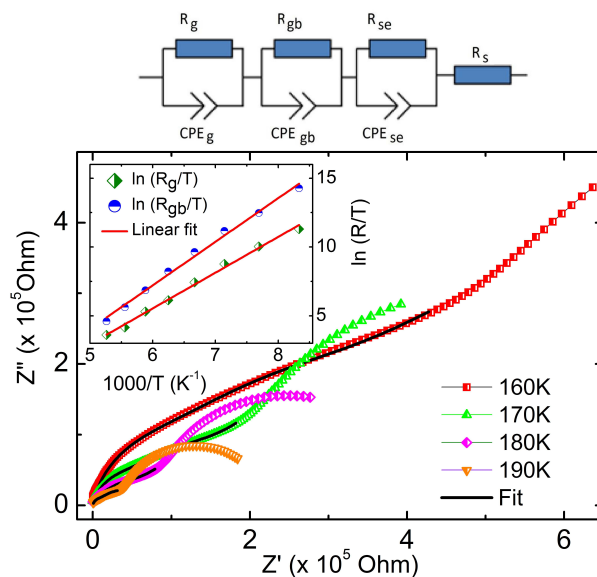

Fig. 10 *Top*: The schematic diagram of the equivalent circuit to model the Nyquist plot. *Bottom*: The experimentally obtained Nyquist plots at four different temperatures and the simulated curves with the equivalent circuit model. Inset shows the SPH model fitting of grain and grain boundary resistances.

ways greater than R_g at a particular temperature which can

be seen in the inset of Fig. 10. The calculated R_g and R_{gb} values at different temperatures obey the SPH model,

$$R = R_0 T \exp(E_a/kT) \tag{11}$$

The activation energy for the grain and grain boundary can be found separately from the fit of corresponding resistances which are 0.22 eV and 0.27 eV respectively.

3.6 Dielectric properties of NFMO50

The relaxation in 50% doped system was studied by investigating the dielectric properties with both frequency and temperature variation. ε_r' and $\tan\delta$ are plotted as a function of temperature in Fig. 11. ε_r' (Fig. 11(a)) shows one relaxation at $150-225$ K and another one at higher temperature. The sharp step-like decrease of ε' and associated relaxation peak of ε'' and $\tan\delta$ shift towards high temperature as frequency is increased is evident in (Fig. 11(b)). Thus, it is considered thermally activated within this temperature range. The dielectric constant $\varepsilon_r(=\varepsilon/\varepsilon_0)$ of a non-ideal system with interaction among dipoles is given by the modified Debye relation,

$$\varepsilon_r = \varepsilon_r' + i\varepsilon_r'' = \varepsilon_{r\infty} + \frac{(\varepsilon_{rs} - \varepsilon_{r\infty})}{1 + (i\omega\tau)^{1-\alpha}} \tag{12}$$

where, τ is the mean relaxation time, $\varepsilon_{r\infty}$ is the dielectric constant at very high frequency (in frequency range 10^{12-15} Hz where only electronic and atomic polarizations contribute) and ε_{rs} is that at static field when polarization is stable. α is a constant. For ideal Debye type relaxation, $\alpha = 0$. $\alpha > 0$ indicates distribution of relaxation which results in a broad peak in dielectric loss. The real and imaginary part can be separated from Eq. 12 as follows;

$$\varepsilon_r' = \varepsilon_{r\infty} + \left(\frac{\Delta\varepsilon_r}{2}\right)\left(1 - \frac{\sinh\beta z}{\cosh\beta z + \cos\frac{\beta\pi}{2}}\right) \tag{13}$$

$$\varepsilon_r'' = \left(\frac{\Delta\varepsilon_r}{2}\right)\left(\frac{\sin\frac{\beta\pi}{2}}{\cosh\beta z + \cos\frac{\beta\pi}{2}}\right) \tag{14}$$

where, $\Delta\varepsilon_r = \varepsilon_{rs} - \varepsilon_{r\infty}$, $z = \ln(\omega\tau)$, and $\beta = (1-\alpha)$. The variation of real parts of the dielectric constant with frequency is shown in Fig.11 (c). The experimental data is fitted with Eq. 13 to estimate α and τ at different temperatures. Since the high frequency region corresponds to contribution from bulk, it is sufficient to fit the high frequency

region only. The relaxation process develops with temperature and follows the SPH model [Fig. 11(d)] which can be expressed as,
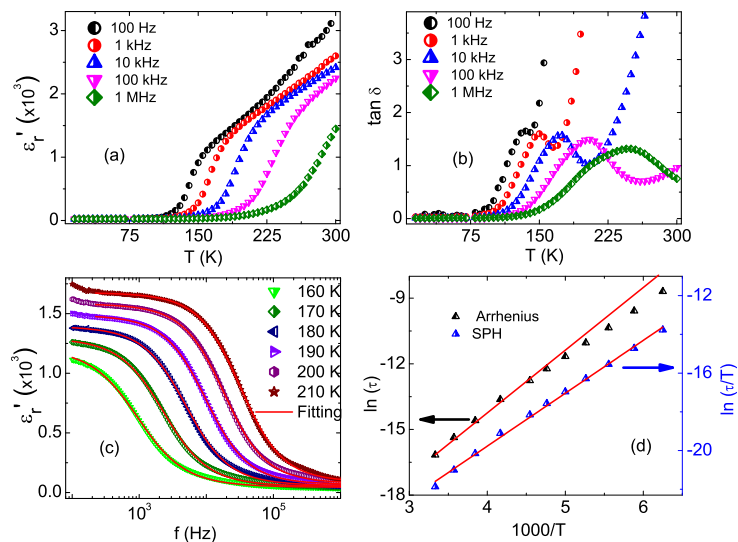
Fig. 11 (a) Dielectric constant vs. temperature. (b) $tan\delta$ vs. temperature showing the peaks associated to the relaxation of dielectric constant. (c) Dielectric constant vs. frequency and the fitting using equation 13. (d) Arrhenius and SPH model plot of τ. τ deviates from Arrhenius type behavior and can be better fitted with SPH model.

$$\tau = \tau_0 T \exp(E_a/kT) \tag{15}$$

where, the pre-exponential factor τ_0 is the high temperature limit of relaxation time and E_a is activation energy. τ clearly deviates from the Arrhenius law $\tau = \tau_0 \exp(E_a/kT)$. For all temperatures, small value of α (< 0.2) indicates that the relaxation dispersion is very small as also the dipole-dipole interaction. The estimated value of the activation energy ($E_a = 0.23$ eV) is close to that obtained previously.

4 summary

In summary, $NdFe_{1-x}Mn_xO_3$ samples were prepared by solid state reaction. All samples are in pure phase and show distorted orthorhombic structure with space group Pbnm. Despite of similar ionic radii of Fe^{3+} and Mn^{3+}, significant changes in lattice parameters are observed with Mn doping. The transition from dynamic to static Jahn-Teller distortion where the staggered orbital order-

ing is supposed to be present, is seen at about 80% of Mn doping level. The samples exhibits high resistivity which decreases with increase in Mn content. The bond angle and bond length in *ab* plane and the activation energies calculated from DC resistivity as well as dielectric relaxations show drastic changes which are attributed to gradual weakening of strong Fe-O-Fe antiferromagnetic superexchange interaction and disappearance of DM interaction at certain threshold doping levels. AC conductivity in 50% doped sample is in conformance to the Jonscher's power law. The contributions of grain and grain boundary are separately visualized with impedance spectroscopy using an equivalent circuit. Dielectric mean relaxation time at different temperatures, obtained by fitting the real part of dielectric constant, are in agreement with the SPH model.

References

1 Y. Moritomo, A. Asamitsu, H. Kuwahara and Y. Tokura, *Nature*, 1996, **380**, 141–144.

2 M. B. Salamon and M. Jaime, *Reviews of Modern Physics*, 2001, **73**, 583.

3 S.-W. Cheong and M. Mostovoy, *Nature materials*, 2007, **6**, 13–20.

4 W. Eerenstein, N. Mathur and J. Scott, *Nature*, 2006, **442**, 759–765.

5 M. Fiebig, *Journal of Physics D: Applied Physics*, 2005, **38**, R123.

6 T. Kimura, *Annu. Rev. Mater. Res.*, 2007, **37**, 387–413.

7 Y. Tokura and S. Seki, *Advanced materials*, 2010, **22**, 1554–1565.

8 V. Laukhin, V. Skumryev, X. Marti, D. Hrabovsky, F. Sánchez, M. García-Cuenca, C. Ferrater, M. Varela, U. Lüders, J. Bobo *et al.*, *Physical review letters*, 2006, **97**, 227201.

9 Y.-H. Chu, L. W. Martin, M. B. Holcomb, M. Gajek, S.-J. Han, Q. He, N. Balke, C.-H. Yang, D. Lee, W. Hu *et al.*, *Nature materials*, 2008, **7**, 478–482.

10 W. Sławiński, R. Przeniosło, I. Sosnowska and E. Suard, *Journal of Physics: Condensed Matter*, 2005, **17**, 4605.

11 L. Chen, T. Li, S. Cao, S. Yuan, F. Hong and J. Zhang, *Journal of Applied Physics*, 2012, **111**, 103905.

12 L. Tsymbal, Y. B. Bazaliy, V. Derkachenko, V. Kamenev, G. Kakazei, F. Palomares and P. Wigen, *Journal of applied physics*, 2007, **101**, 123919.

13 S. Yuan, W. Ren, F. Hong, Y. Wang, J. Zhang, L. Bellaiche, S. Cao and G. Cao, *Physical Review B*, 2013, **87**, 184405.

14 J. B. Goodenough, *Magnetism and chemical bond*, Interscience publishers Technical Report 186, 1963.

15 J. B. Goodenough, *Physical Review*, 1955, **100**, 564.

16 J.-S. Zhou and J. Goodenough, *Physical review letters*, 2006, **96**, 247202.

17 F. Moussa, M. Hennion, J. Rodriguez-Carvajal, H. Moudden, L. Pinsard and A. Revcolevschi, *Physical Review B*, 1996, **54**, 15149.

18 T. Kimura, S. Ishihara, H. Shintani, T. Arima, K. Takahashi, K. Ishizaka and Y. Tokura, *Physical Review B*, 2003, **68**, 060403.

19 J. Zhang, X. Lu, J. Zhou, J. Su, K. Min, F. Huang and J. Zhu, *Physical Review B*, 2010, **82**, 224413.

20 Y.-H. Huang, M. Karppinen, N. Imamura, H. Yamauchi and J. B. Goodenough, *Physical Review B*, 2007, **76**, 174405.

21 F. Hong, Z. Cheng, S. Zhang and X. Wang, *Journal of Applied Physics*, 2012, **111**, 034104.

22 C. Ang, Z. Yu and L. Cross, *Physical Review B*, 2000, **62**, 228.

23 O. De Lima, J. Coaquira, R. De Almeida, L. De Carvalho and S. Malik, *Journal of Applied Physics*, 2009, **105**, 013907.

24 W. Tong, B. Zhang, S. Tan and Y. Zhang, *Physical Review B*, 2004, **70**, 014422.

25 Z. Yu, C. Ang, P. Vilarinho, P. Mantas and J. Baptista, *Journal of applied physics*, 1998, **83**, 4874–4877.

26 O. Bidault, P. Goux, M. Kchikech, M. Belkaoumi and M. Maglione, *Physical Review B*, 1994, **49**, 7868.

27 L. Zhang and Z.-J. Tang, *Physical Review B*, 2004, **70**, 174306.

28 C. Ganeshraj, S. Kavita, R. Mahendiran, N. Sharma, A. Das and P. Santhosh, *Applied Physics Letters*, 2013, **103**, 112909.

29 Y. Sun, X. Xu and Y. Zhang, *Journal of Physics: Condensed Matter*, 2000, **12**, 10475.

30 J. Kanamori, *Journal of Physics and Chemistry of Solids*, 1959, **10**, 87–98.

31 J. B. Goodenough, *Journal of Physics and chemistry of Solids*, 1958, **6**, 287–297.

32 J. Van Den Brink and D. I. Khomskii, *Journal of Physics: Condensed Matter*, 2008, **20**, 434217.

33 A. K. Jonscher, *Universal relaxation law: a sequel to Dielectric relaxation in solids*, Chelsea Dielectrics Press, 1996.

34 H. Nhalil, H. S. Nair, H. Bhat and S. Elizabeth, *EPL (Europhysics Letters)*, 2013, **104**, 67002.

35 J. T. Irvine, D. C. Sinclair and A. R. West, *Advanced Materials*, 1990, **2**, 132–138.